Single-Crystalline Colloidal Quasi-2D Tin Telluride

Fu Li, Jiecai Fu, Abderrezak Torche, Sascha Kull, Andreas Kornowski, Rostyslav Lesyuk, Gabriel Bester, and Christian Klinke*

Tin telluride is a narrow-gap semiconductor with promising properties for infrared (IR) optical applications and topological insulators. A convenient colloidal synthesis of quasi-2D SnTe nanocrystals through the hot-injection method in a nonpolar solvent is reported. By introducing the halide alkane 1-bromotetradecane as well as oleic acid and trioctylphosphine, the thickness of 2D SnTe nanostripes can be tuned down to 30 nm, while the lateral dimensional can reach 6 µm. The obtained SnTe nanostripes are single crystalline with a rock-salt crystal structure. The absorption spectra demonstrate pronounced absorption features in the IR range revealing the effect of quantum confinement in such structures.

1. Introduction

Owing to the high potential for infrared (IR) and near-infrared detectors, solar cells and thermoelectric applications, narrow-bandgap semiconductor nanocrystals have triggered intensive investigations in the recent years.[1–6] Tin telluride (SnTe), as a IV–VI narrow bandgap semiconductor (0.18 eV, bulk), has a rock-salt crystal structure ($Fm\overline{3}m$) with mirror symmetry in contrast to other tin chalcogenides (SnS and SnSe) with orthorhombic layered crystal structure.[7,8] SnTe has also been considered as a remarkable topological crystalline insulator (TCI) based on its crystal symmetry, and it has a potential for mid-IR applications, as well as photovoltaic devices.[9–12] So far, attempts to obtain solution-based SnTe nanocrystals (NCs) only yielded 0D or 1D nanostructures.[13–15] Here, we report a synthesis protocol for large and thin SnTe nanosheets and nanostripes with high crystallinity and the thicknesses down to 30 nm and largest lateral sizes of up to 6 µm. To the best of our knowledge, this is the first instance for 2D colloidal SnTe nanostructures. The obtained nanocrystals have been investigated by means of transmission electron microscope (TEM), high resolution TEM, powder X-ray diffraction (XRD), selected area electron diffraction pattern (SAED), atomic force microscopy (AFM), energy-dispersive X-ray (EDX) analysis, and Fourier transform infrared (FTIR) measurements. The absorption spectra of nanosheets and nanostripes in ensemble showing distinct features in the mid-infrared are rationalized with the support of density functional theory calculations.

2. Results and Discussion

As a nonflammable and reactive Sn(II) precursor, tin acetate was used together with elemental Te dissolved in trioctylphosphine. In a typical synthesis, 0.25 mmol tin(II) acetate (TA), 6.4 mmol oleic acid (OA), and 1.0 mmol trioctylphosphine (TOP) were mixed with 10 mL diphenyl ether (DPE) as solvent. After degassing the solution at 75 °C for 2 h, 1-bromotetradecane (1-BTD) was added as Br source, followed by heating the system to the reaction temperature of 250 °C. Following the fast injection of the Te precursor (TOP-Te), the reaction changed color rapidly from yellow to grayish yellow. After the color change, the

Dr. F. Li, Dr. A. Torche, Dr. S. Kull, A. Kornowski, Dr. R. Lesyuk,
Prof. G. Bester, Prof. C. Klinke
Institute of Physical Chemistry
University of Hamburg
Martin-Luther-King-Platz 6, Hamburg 20146, Germany
E-mail: christian.klinke@uni-rostock.de

Dr. J. Fu
Key Laboratory for Magnetism and Magnetic Materials of the Ministry
of Education
School of Physical Science and Technology
Lanzhou University
Lanzhou 730000, P. R. China

Dr. R. Lesyuk, Prof. C. Klinke
Institute of Physics
University of Rostock
Albert-Einstein-Strasse 23, Rostock 18059, Germany

Dr. R. Lesyuk
Pidstryhach Institute for Applied Problems of Mechanics and
Mathematics of NAS of Ukraine
Naukowa Str. 3b, Lviv 79060, Ukraine

Dr. R. Lesyuk
Department of Photonics
Lviv Polytechnic National University
Bandery Str. 12, Lviv 79000, Ukraine

Prof. C. Klinke
Department of Chemistry
Swansea University–Singleton Park
Swansea SA2 8PP, UK
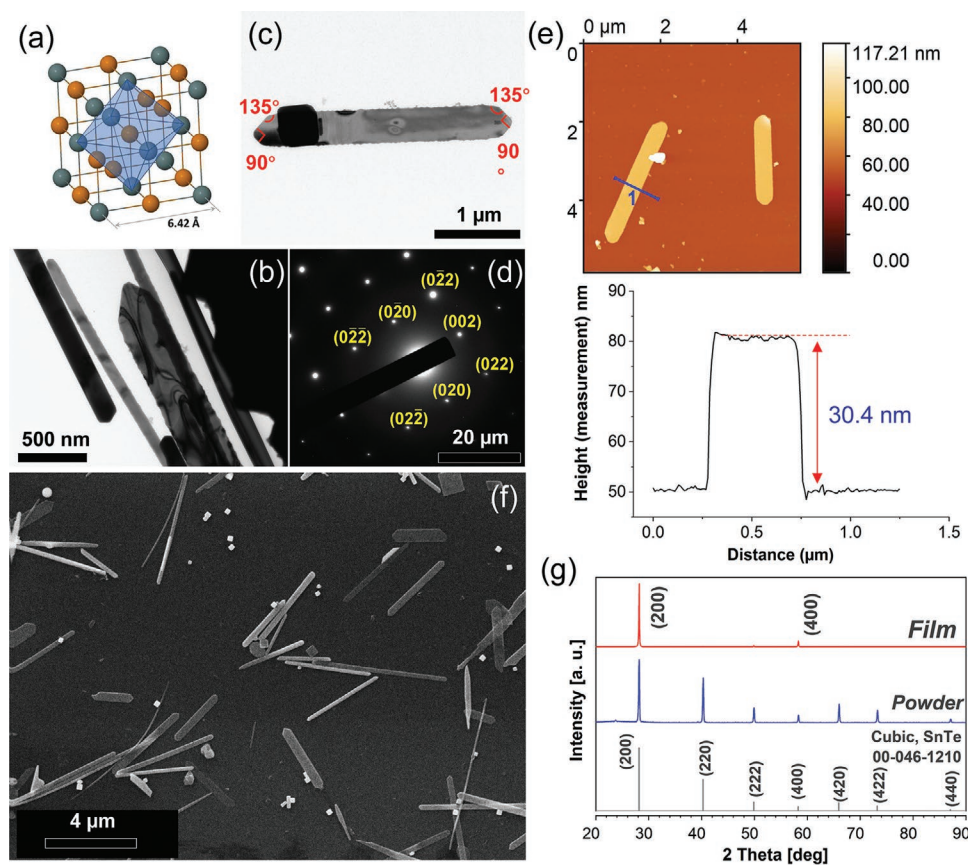
Figure 1. a) Face-centered cubic unit cell (rock-salt structure) of β-SnTe (gray: Sn; orange: Te). Each cation is coordinated by six anions forming a coordination octahedron. b,c) TEM image of SnTe NSPs using the standard synthesis process. d) SAED pattern of a SnTe single NSP. e) AFM image and height profile of a SnTe NSP. f) SEM image of SnTe NSPs, NPs and NRs. g) XRD patterns of drop-casted sample (top), sample in capillary tube (center) and of SnTe NCs, and literature stick pattern (bottom).

reaction solution was cooled down to room temperature, followed by purification and storage in toluene.

The as-synthesized 2D SnTe nanocrystals (NCs) consist mainly of 2D nanostripes (NSPs), and some stick-shaped nanocrystals (SNCs) (**Figure 1**). As a side product, cubic SnTe nanoparticles (NPs) can be observed as well. A typical unit cell of the cubic phase of β-SnTe is shown in Figure 1a.[16,17] Figure 1b–e shows typical TEM images, SAED, and an AFM image of the SnTe NSPs prepared at a reaction time of 250 °C for 1.5 min. The stripes can range from 1.5 to 5.8 μm in length with a mean length of 3.2 μm derived from the scanning electron microscope (SEM) images (Figure 1f). The SAED patterns shown in Figure 1d display well-defined dot patterns representing the planes of $(0\bar{2}\bar{2})$, $(0\bar{2}0)$, $(0\bar{2}2)$, (002), (022), (020), and $(02\bar{2})$ of a single SnTe NSP (zone axis $\langle 100 \rangle$). This demonstrates that the obtained SnTe NSPs are single-crystalline and single-phase structures. The AFM image and the corresponding height analysis show that the SnTe NSP has a flat surface morphology and the thickness of ≈30 nm (Figure 1e). Powder X-ray diffraction (Figure 1g) for the sample collected in a capillary demonstrates that all the diffraction peaks can be indexed as cubic crystal structure of SnTe ($Fm\bar{3}m$, 225, 00-046-1210), while the XRD pattern of the drop-casted sample exhibits pronounced reflexes of (200) and (400) due to the texture effect. This implies that the NSPs lay perpendicular to the [100] direction, which is defined

here as the thickness direction. In addition, the measured angles between the tip edges are 135° and between a tip edge and a side edge 90°, as will be explain later in the text (Figure 1c).

High resolution TEM (HRTEM) characterizations of SnTe NSPs and SnTe NPs, together with the corresponding fast Fourier transform (FFT) analysis were performed as shown in **Figure 2**, displaying the crystallography, exposed facets and the growth direction of SnTe NSPs (main product) and NPs (byproduct). The measured lattice spacing of ≈0.32 nm, which are perpendicular, confirms the two perpendicular in-plane facets (002) and (020) belong to the {100} family (Figure 2b,c). With the already-known angles from Figure 1c and the crystal orientation, the right-angled edges of the NSP can be determined to be parallel to the (010) and (001), as well as their parallel facets $(0\bar{1}0)$ and $(00\bar{1})$. Based on FFT analysis, we deduct that the long axis points along the [011] or $[0\bar{1}1]$ directions and the analysis of according HRTEM images yields a lattice spacing of 0.227 nm (Figure 2b–f). An energy-dispersive X-ray (EDX) line scan analysis of the NSP (Figure S1a, Supporting Information) and the corresponding EDX element analysis (Figure S2, Supporting Information) yield a highly stoichiometric ratio of Sn to Te (1:1), and also a small amount of oxygen in the SnTe NSPs and NPs. EDX mapping also confirmed an even distribution of the elements tin, tellurium, and on the surface located oxygen, which is clearly recognizable as a layer
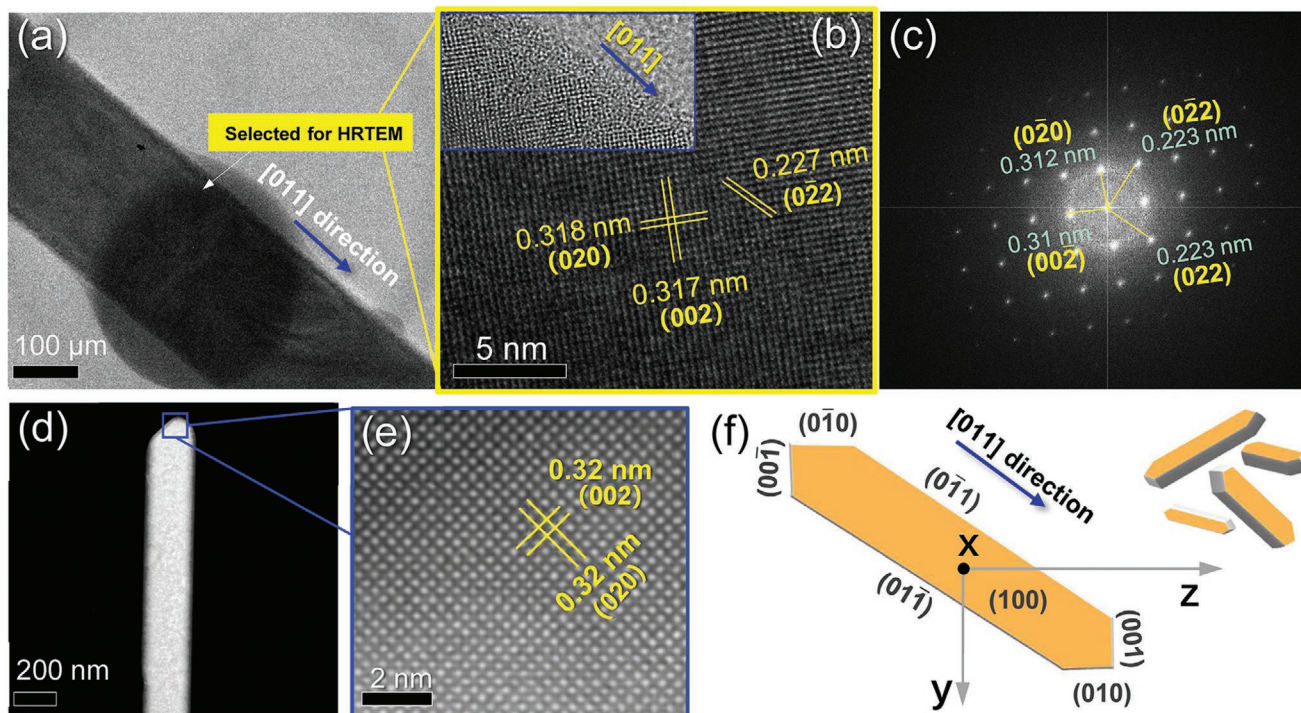
Figure 2. HRTEM characterizations of SnTe NSPs and the corresponding FFT analysis a–c). d,e) STEM characterization of the right-angled edges of the SnTe NSP. f) Schematic representation of SnS NSP.

around the SnTe particle (Figure S1b,c, Supporting Information). The origin of this oxide layer could be a result of surfactants like oleic acid and/or acetate, a weak oxidation of tellurium, tin tellurate, or a SnO_X shell founded on SnTe nanocubes reported by Guo et al.[13] However, in HRTEM images we can clearly see areas with interrupted fringes appearing amorphous (Figure 2b, inset). A uniform distribution of a small amount of oxygen through the nanostripe was also found in the line-scan profile in Figure S1 (Supporting Information), indicating the presence of oxygen on the SnTe nanostripes as well. Based on the EDX mapping data, the sizes of the mapping images of element Sn and O are slightly larger than that of element Te, implying that the phenomenon of a SnO_X shell on SnTe NCs. This shell might protect the synthesized SnTe nanocrystals from being oxidized further, giving the nanocrystals more stability, which is already demonstrated by Guo et al.[13]

The morphology evolution was investigated by taking aliquots during the reaction followed by TEM and SAED analysis (Figure S3, Supporting Information). At the early stages, before 30 s, there are no defined nanostructures with cubic phase observed, only SnO_2 nanostructures are found as confirmed by SAED and TEM characterization (Figure S4, Supporting Information). The SAED pattern indicates the SnO_2 nanostructures align already during the first stages of the synthesis, which may hint to oriented attachment as growth mechanism of the earlier-formed SnO_2 particles.[18,19] Afterward, the SnTe NSPs with defined shape (≈2 µm length, 100–180 nm width) form within the first minute of the reaction (Figure S3c, Supporting Information). As the reaction proceeds, the NSPs grow longer and the widths become larger. The largest of them reach 3.8 and 1.2 µm in length and in width respectively after 3.5 min of

reaction (Figure S3e, Supporting Information). In addition, a small fraction of particles was also formed with the same cubic phase. The SnO_2 product is assumed to origin from the introduction of a tiny amount of oxygen when injecting 1-BTD during the reaction (5 s after hot injection). Its formation is assumed to be independent from the nucleation and growth of SnTe nanocrystals afterward (1 min after hot injection). The TEM analyses provide a possible clue for the formation of SnTe NSPs. The fast nucleation occurs after the hot injection of the tellurium precursor, followed by the anisotropic growth process based on different growth speed on different facets, finally forming the defined morphology.[20,21]

As promising symmetry-breaking ligands for colloidal nanocrystal syntheses, halide ions have some advantages such as relatively high electronegativities and reactivities.[22–25] For comparison, reference syntheses without 1-BTD were also performed (Figure S5, Supporting Information). However, there are only agglomerates produced if no 1-BTD was used during the synthesis. We found that the amount of 1-bromotetradecane (1-BTD) is one of the key factors for obtaining relative uniform and well-defined 2D SnTe NSPs. The amount of 1-BTD as structure giving factor was studied to investigate the influence of the halide ligand on the synthesis and to find the optimal amount to obtain 2D NSPs (**Figure 3**). It demonstrates that irregular-shaped platelets are formed together with long SNCs and NPs instead of well-defined NSPs, when the 1-BTD amount is less than 0.64 mmol (Figure 3a,b). When the amount reaches 0.64 mmol, most of the product is composed of NSPs together with a few NRs and cubic NPs (Figure 3c). This indicates that small amounts of 1-BTD together with OA and TOP as ligands will passivate the {100} facets, impelling the nuclei to favor the formation of
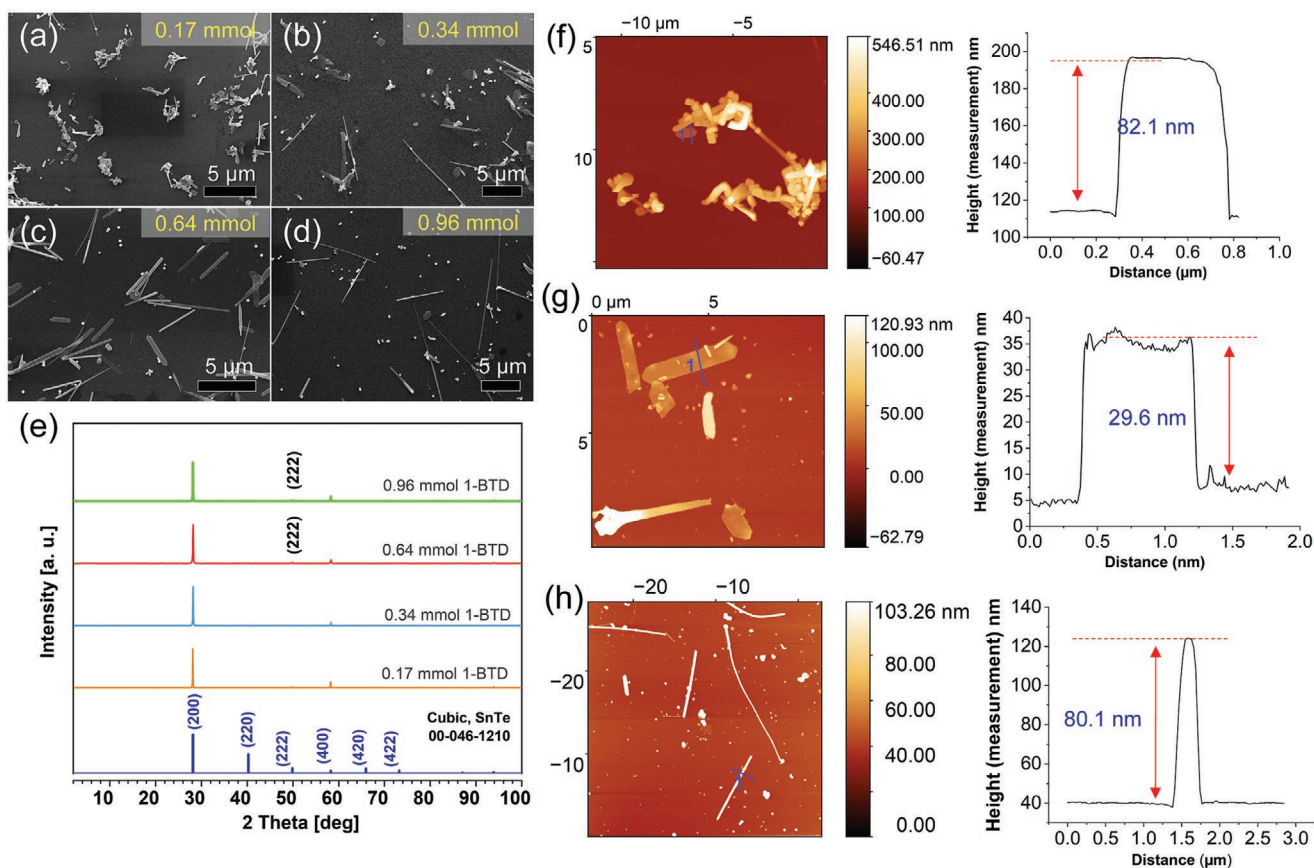
Figure 3. SEM images of SnTe nanostructures prepared with different amounts of 1-BTD: a) 0.17 mmol, b) 0.34 mmol, c) 0.64 mmol, and d) 0.96 mmol. e) XRD diffractograms of the samples in (a)–(d). f–h) AFM images and height measurements of the synthesized SnTe nanostructures from Figure 3(a), (b), and (d).

NSPs with right-angled edges and small height compared to the large lateral size (Figure 2f,h). Larger amounts of 1-BTD lead to a larger number of long rods (or wires) (Figure 3d). This may result from the replacement of other ligands by stronger X-type ligand (Br$^-$) and destabilization of the {100} facets and faster growth along the [011] direction. The corresponding XRD diffractograms show strong texture effect (Figure 3e).

AFM measurements show that the NSPs synthesized with 0.34 mmol of 1-BTD possess similar thicknesses (around 30 nm, Figure 3g) as the ones with 0.64 mmol 1-BTD, which is the standard synthesis (Figure 1e), while long stick-shaped nanocrystals are synthesized with 0.96 mmol 1-BTD (thickness around 80 nm; Figure 3h). These long sticks possess similar diameters as the ones obtained in the standard synthesis (≈90 nm in thickness; Figure S6, Supporting Information).

In contrast to the synthesis with the assistance of 1-BTD, the reaction in the presence of 1-CTD leads to the formation of NSs beside NSPs. We found that 1-chlorotetradecane (1-CTD) could also assist to form 2D SnTe nanostructures (Figure S7, Supporting Information). The reaction temperature was found to be optimal in the range of 220–260 °C for NS/NSP formation. When the synthesis temperature was lowered to 220 °C in the case of BTD the nanostripe shape still dominates in the product (Figure S9, Supporting Information). By varying the reaction temperature between 220 and 260 °C, in the CTD assisted synthesis we can observe a tendency more clearly. The

2D nanostructure shape evolves from thick squares or irregular shapes (112.7 nm, Figure S7a, Supporting Information), to thick elongated stripe-like shapes (99.1 nm; Figure S7b, Supporting Information). All the XRD diffractograms for these samples display pronounced (200) and (400) reflexes representing strong texture effect (Figure S8, Supporting Information). The reason for obtaining the product synthesized by using chloride alkanes can be explained by the nucleophilicity difference of Cl$^-$ and Br$^-$ ions (Cl$^-$ < Br$^-$). The slower ion release will occur with Cl$^-$ compared to Br$^-$, based on their ion sizes to produce lower amounts of ions available at the early stages of the reaction, in particular at lower temperature (220 °C). It will then result in a less dense coverage on each facet, which leads to a smaller degree of growth anisotropy for the nanocrystals. Hence, the synthesis with 1-CTD shows a lower yield of 2D morphology with more 3D NPs instead (Figure S7, Supporting Information).

As has been found earlier, halogen alkanes units and their corresponding released halide ions can be both found on the surface of 2D nanoparticles when halide alkanes are adopted as ligands in the reaction.[26] In order to decouple the possible effect of two species in our synthesis, we introduced the halogens in the complex with tin precursors using the tin chloride precursor instead of tin acetate. It showed that 2D SnTe nanostructures can be also obtained (Figure S10, Supporting Information). This supports the argument about the key role of the halogen ions in breaking the symmetry during the nucleation

ADVANCED
SCIENCE NEWS
www.advancedsciencenews.com

ADVANCED
MATERIALS
INTERFACES
www.advmatinterfaces.de

and growth of the 2D SnTe NCs. More than half of the nanocrystals are etched after collection from the synthesis, which is independent of the amount of tin precursor in the reaction. Tin(II) bromide can also lead to similar products as tin(II) chloride (Figure S11, Supporting Information). The AFM characterization shows that the thickness is around 76 nm (Figure S12, Supporting Information). We note a strong etching effect, which appears at the beginning of NS formation (Figure S13, Supporting Information). The taking-aliquot experiment indicates that the etching by halide ions happens rapidly from the very beginning during the formation of NSs. As known, halide ions released from halide alkanes are the actually functioning ligands instead of the original halide alkanes themselves in IV–VIA group semiconductors.[27] By means of the specific binding preference on crystal surfaces, or the complexation with metal atoms, or the etching process, halide ions have been proven as good optional ligands for obtaining 2D nanostructures in solution.[22,24,28] Further, we found that for the NS formation, halide ions can be introduced from salts such as LiCl or LiBr dissolved in dimethylformamide (DMF) and added to the reaction flask (Figure S14, Supporting Information). However, in this case, along with NSs we observe structures with undefined or disturbed 2D morphology. Therefore, the involvement of halide ions, especially halogen alkanes is proven to be vital for the symmetry breaking in 2D cubic-phase SnTe nanocrystal synthesis. Further, we can conclude that alkane chains in the syntheses with halide alkanes play an important role in stabilizing nanocrystals during the reaction, avoiding the formation of agglomerates and avoiding the etching process.

Note that the occurrence of the etching on SnTe is assumed to be mainly due to the change of the chemical environment when the tin chloride/bromide is used.[27] The salt addition into the reaction can affect the polarity of the solvent. Further, it also alters the capping conditions of the organic ligand layers on the crystal surface, which triggers the etching process when the ligand layer conditions change, followed by a change of the solubility of SnTe. This enables the dissolution of SnTe at the very early stage of the growth after the sheets form in the case of using tin chloride/bromide or LiCl/LiBr.

The absorption spectra of SnTe nanostructures obtained with different halide sources recorded by Fourier-transform infrared (FTIR) spectroscopy are shown in **Figure 4**. We find pronounced features in the mid-IR range. It has been reported that oleic acid has an absorption band from 3000 to 4000 nm ($\approx$410–310 meV)[14], which we think is responsible for the observed peaks at 0.33, 0.36, and 0.4 eV. Both NSs and NSPs demonstrate three strong absorption peaks at 230, 260, and 290 meV, from which the latter two features show the same shape and position in the three samples. This latter observation suggests that the two peaks at 260 and 290 meV are potentially structure independent as they do not show confinement effect and no shape change. The first absorption peak at around 230 meV is however blueshifted in the 30 nm nanostripes by 20 meV as compared to the 80 nm NSs and also shows a change in the shape indicating that it is potentially a structure dependent peak. In order to get more insights about the measured spectra, we calculated the absorption spectrum of bulk SnTe using the independent-particle approximation (i.e., no excitonic effects) using fully relativistic (i.e., including spin–orbit interaction) density functional theory (DFT) calculation at the PBE level as implemented in the Quantum-espresso package.[29] Unfortunately, the ab-initio simulation of a 30 nm SnTe slab is prohibitively expensive and cannot be performed. Based on the band structure (see Figure 4e), we note that bulk SnTe is an L-point direct bandgap semiconductor where in the range 0.0–1.0 eV only the valence band maximum (VBM or $1S_h$) and the conduction band minimum (CBM or $1S_e$), CBM+1, and CBM+2 contribute to the optical spectrum. Moreover, in contrast to standard Γ-point semiconductors (such as CdSe, ZnS, etc.), bands with heavy hole, light hole, and split-off character are absent near the Fermi level around the L point in SnTe. The theoretical optical spectrum (Figure 4d) of bulk SnTe shows only one absorption peak in the range 0.0–0.5 eV, which corresponds to the fundamental $1S_h$–$1S_e$ transition in bulk SnTe.
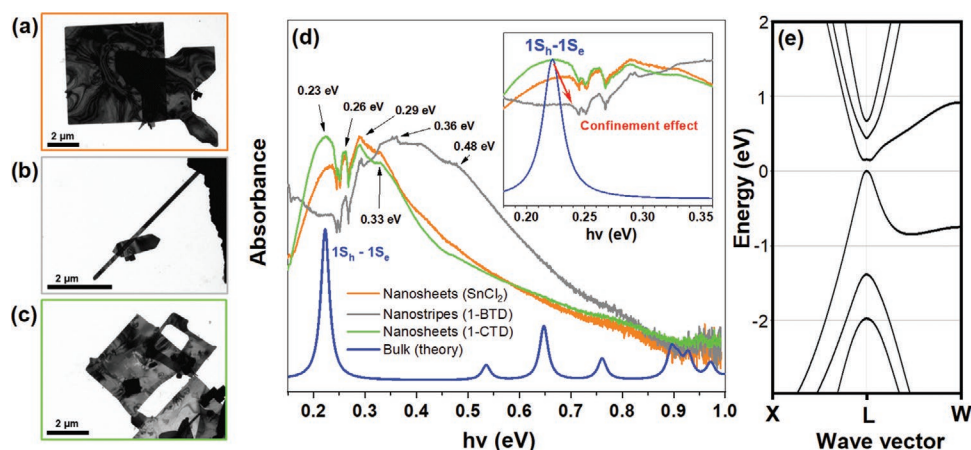
Figure 4. Optical absorption spectra of SnTe nanosheets and nanostripes synthesized respectively using different halides and halide sources: TEM images of SnCl$_2$ as precursor a), 1-BTD molecules as halide ligands b), and 1-CTD molecules as halide ligands c). d) Comparison between experimental spectra (orange, green, and gray) for nanosheets and nanostripes with theoretical (DFT-PBE) bulk absorption (in blue) where we see no absorption peaks in the range 0–0.5 eV except the $1S_h$–$1S_e$ transition (the range 0.15–0.35 eV magnified in the inset). Note that the first theoretical absorption peak has been blueshifted to match the first experimental absorption feature in nanosheets a); e) calculated electronic bands structure of bulk SnTe near the L-point, the Fermi level is set to 0.

Since the Bohr radius of the bulk SnTe is 95 nm, lowering the thickness up to 80 and 30 nm results in a blueshift of this fundamental transition to match the first observed peak in the 80 and 30 nm NSs and nanostripes, respectively.[13] The absence of other absorption peaks in the range 0.0–0.5 eV confirms further that two peaks at 260 and 290 meV are potentially due to ligand, defect, or surface trapped states. To verify whether they can also be due to higher excitonic transitions (which are not described in our actual calculation) as suggested by previous works,[13,14] we later calculate the exciton Rydberg energy for SnTe. Using the effective mass approximation to describe the 1D confinement in NSs and nanostripes, the change in the bandgap (E_g) in theses nanostructures as compared to the bulk value is given by $\Delta(L) = \pi^2 * \frac{\hbar^2}{2 * \mu * L^2}$, with $m_{eff} = 0.036 \cdot m_0$, and L being the reduced electron–hole effective mass and the thickness of the simulated slab respectively (m_0 is the free electron mass). Note that the effective mass in SnTe is highly anisotropic and nonparabolic;[30] however, this should not affect the qualitative description of the optical spectra adopted here within the effective mass approximation. DFT-PBE calculations with spin–orbit yield a hole effective mass of 0.13 in the L–W direction and 0.27 in the L–X direction while for the electron it is 0.046 and 0.042 in the L–W and L–X directions, respectively (atomic units are used). This gives an averaged electron–hole mass of $0.036 \cdot m_0$ and the corresponding change in the bandgap is then 12 meV for nanostripes of 30 nm thickness and only 1.5 meV for NSs with 80 nm. The difference being 10 meV is in qualitative agreement with the experimental value of 20 meV, which corresponds to the blueshift of the first absorption in nanostripes as compared to NSs. This reveals the effect of quantum confinement in thinner nanostructures.

Based on the values for effective charge carrier masses we further calculate the exciton Rydberg energy for SnTe: $R_X = \mu/(m_0 \xi_r^2) R_H$, where μ is the reduced mass calculated above, m_0 is the electron mass, ξ_r is the static dielectric constant, and R_H is the Rydberg energy of the hydrogen atom (13.6 eV). With the value of $\xi_r = 1770$,[31] $R_X = 1.6 \times 10^{-7}$ eV. The energy difference between the first and second excitonic transitions will be $E_2^{exc} - E_1^{exc} = \frac{3}{4} R_X$ derived from the expression for the exciton energy $E_n^{exc} = E_g - \frac{R}{n^2}$, with $n = 1, 2, 3, ...$ Thus, the further observed transitions after the $1S_h$–$1S_e$ (at 0.26, 0.29, and 0.36 eV) cannot be attributed to the series of excitonic states. With such a tiny R_X these transitions could be resolved neither at room temperature nor at usual cryogenic temperatures. Further, the hypothetical appearance of plasmonic resonances was suggested by Gou et al.[13] based on a self-doping effect. In our case the stoichiometry of 1:1 (Sn:Te) was found and we rather exclude the plasmonic resonances in this range of wavelengths.

3. Conclusion

We demonstrated the first colloidal synthesis approach of quasi-2D SnTe nanocrystals with narrow bandgap. The introduction of halide alkanes to the synthesis of cubic-phase SnTe nanocrystals in solution might provide a means to also manipulate other 2D nanocrystal syntheses, such as for HgTe. The small thickness (down to 30 nm) and the large lateral size

(6 μm) with high crystallinity, and the colloidal approach manifests a promising outlook of theses nanomaterials in infrared optical applications, electronic or optoelectronic devices, as well as low-dimensional topological insulators.

4. Experimental Section

Chemicals and Materials: Oleic acid (OA, 90%), trioctylphosphine (TOP, 97%), diphenyl ether (DPE, ≥99%), 1-bromotetradecane (1-BTD, 97%), 1-chlorotetradecane (1-CTD, 98%), N,N-dimethylformamide (DMF, pharmaceutical secondary standard), lithium chloride (LiCl, anhydrous, ≥99%), tin(II) bromide ($SnBr_2$), and toluene were purchased from Sigma-Aldrich. Tin(II) acetate (Sn (CH_3CO_2)$_2$, anhydrous, ≥99.99%) and tellurium powder (Te, 99.997%) were purchased from Alfa Aesar. Tin(II) chloride ($SnCl_2$, ≥99.99%) was purchased from Thermo Fisher Scientific. All the chemicals were used as-received without additional purification. Trioctylphosphine-Te (TOP-Te) was prepared and stored in a glovebox and all the syntheses were carried out applying standard air-free Schlenk-line techniques.

Material Characterization: Transmission electron microscope (TEM) images and selected area electron diffraction (SAED) patterns were obtained using a TEM with the type of JEOL-1011(LaB$_6$, 100 kV). Samples for TEM measurements were prepared by dropping a 10 μL diluted toluene dispersion onto carbon-coated TEM grids. Atomic-resolved images were recorded by a probe-corrected high-angle annular dark-field scanning transmission electron microscopy (HAADF-STEM, FEI Themis Cubed 300) with a probe semiconvergence angle of 24.7 mrad and collect angle range of 70–200 mrad. To avoid beam damage, the atomic HAADF-STEM image was obtained by an image series composed of 16 fast exposure images of the same region following by a postacquisition image distortion correction and averaging (Smart Align).[32] The high-resolution (HR) TEM images were performed on a double corrected (CETCORR and CESCORR, CEOS) JEOL 2200 FS operating at 200 kV. Scanning electron microscopy (SEM, LEO 1550) was also applied for morphology information of SnTe nanocrystals. Wide-angle powder X-ray diffraction (XRD) patterns were collected using a Philips X'Pert X-ray diffractometer with Cu Kα radiation (λ = 0.154 nm). Fourier transform infrared (FTIR) measurements were carried out by drying the nanocrystals and putting the powders on a diamond-ATR unit (Bruker VERTEX 70). The FTIR measurements are performed with a range from 400 to 8000 cm^{-1}.

Synthesis of 2D SnTe Nanosheets: In a typical synthesis of SnTe NSs, Sn (CH_3CO_2)$_2$ (TA, 0.25 mmol), oleic acid (OA, 2.0 mL), trioctylphosphine (TOP, 0.5 mL), and diphenyl ether (DPE, 10 mL) were mixed and dissolved in a 50 mL three-neck flask, then dried and degassed under vacuum at 75 °C for 120 min. The solution was then heated to reaction temperature 250 °C after adding certain amount of 1-bromotetradecane (1-BTD), followed by the rapid injection of 1 M TOP-Te precursor solution. The heating mantle was removed when the solution color changed from yellow to grayish yellow. The resultant nanostructures were then purified by centrifugation with toluene at 4000 rpm for 3 min (2–3 times). The product could then be resuspended in toluene for further characterization or storage.

Supporting Information

Supporting Information is available from the Wiley Online Library or from the author.

Acknowledgements

Conflict of Interest

The authors declare no conflict of interest.

Keywords

[1] L. Sun, J. J. Choi, D. Stachnik, A. C. Bartnik, B.-R. Hyun, G. G. Malliaras, T. Hanrath, F. W. Wise, *Nat. Nanotechnol.* **2012**, *7*, 369.

[2] Y. Du, B. Xu, T. Fu, M. Cai, F. Li, Y. Zhang, Q. Wang, *J. Am. Chem. Soc.* **2010**, *132*, 1470.

[3] M. C. Beard, J. M. Luther, A. J. Nozik, *Nat. Nanotechnol.* **2014**, *9*, 951.

[4] M. Ibáñez, R. Zamani, A. LaLonde, D. Cadavid, W. Li, A. Shavel, J. Arbiol, J. R. Morante, S. Gorsse, G. J. Snyder, *J. Am. Chem. Soc.* **2012**, *134*, 4060.

[5] J. S. Liu, X. H. Li, Y. X. Guo, A. Qyyum, Z. J. Shi, T. C. Feng, Y. Zhang, C. X. Jiang, X. F. Liu, *Small* **2019**, *15*, 1902811.

[6] J. Feng, X. Li, Z. Shi, C. Zheng, X. Li, D. Leng, Y. Wang, J. Liu, L. Zhu, *Adv. Opt. Mater.* **2020**, *8*, 1901762.

[7] M. Safdar, Q. Wang, M. Mirza, Z. Wang, K. Xu, J. He, *Nano Lett.* **2013**, *13*, 5344.

[8] T. Feng, D. Zhang, X. Li, Q. Abdul, Z. Shi, J. Lu, P. Guo, Y. Zhang, J. Liu, Q. J. Wang, *ACS Appl. Nano Mater.* **2020**, *3*, 674.

[9] T. H. Hsieh, H. Lin, J. Liu, W. Duan, A. Bansil, L. Fu, *Nat. Commun.* **2012**, *3*, 982.

[10] Y. Tanaka, Z. Ren, T. Sato, K. Nakayama, S. Souma, T. Takahashi, K. Segawa, Y. Ando, *Nat. Phys.* **2012**, *8*, 800.

[11] J. Shen, Y. Jung, A. S. Disa, F. J. Walker, C. H. Ahn, J. J. Cha, *Nano Lett.* **2014**, *14*, 4183.

[12] Z. Li, S. Shao, N. Li, K. McCall, J. Wang, S. X. Zhang, *Nano Lett.* **2013**, *13*, 5443.

[13] S. Guo, A. F. Fidler, K. He, D. Su, G. Chen, Q. Lin, J. M. Pietryga, V. I. Klimov, *J. Am. Chem. Soc.* **2015**, *137*, 15074.

[14] M. V. Kovalenko, W. Heiss, E. V. Shevchenko, J.-S. Lee, H. Schwinghammer, A. P. Alivisatos, D. V. Talapin, *J. Am. Chem. Soc.* **2007**, *129*, 11354.

[15] H. D. Jin, C.-H. Chang, *J. Mater. Chem.* **2011**, *21*, 12218.

[16] K. Chang, T. P. Kaloni, H. Lin, A. Bedoya-Pinto, A. K. Pandeya, I. Kostanovskiy, K. Zhao, Y. Zhong, X. Hu, Q. K. Xue, *Adv. Mater.* **2019**, *31*, 1804428.

[17] B. Dong, Z. Wang, N. T. Hung, A. R. Oganov, T. Yang, R. Saito, Z. Zhang, *Phys. Rev. Mater.* **2019**, *3*, 013405.

[18] D. G. Stroppa, L. A. Montoro, A. Beltran, T. G. Conti, R. O. Da Silva, J. Andres, E. R. Leite, A. J. Ramirez, *Chem. Commun.* **2011**, *47*, 3117.

[19] W. Wan, Y. Li, X. Ren, Y. Zhao, F. Gao, H. Zhao, *Nanomaterials* **2018**, *8*, 112.

[20] F. Li, M. M. R. Moayed, F. Gerdes, S. Kull, E. Klein, R. Lesyuk, C. Klinke, *J. Mater. Chem. C* **2018**, *6*, 9410.

[21] F. Li, M. M. Ramin Moayed, E. Klein, R. Lesyuk, C. Klinke, *J. Phys. Chem. Lett.* **2019**, *10*, 993.

[22] S. Ghosh, L. Manna, *Chem. Rev.* **2018**, *118*, 7804.

[23] M. Grzelczak, J. Pérez-Juste, P. Mulvaney, L. M. Liz-Marzán, *Chem. Soc. Rev.* **2008**, *37*, 1783.

[24] F. Gerdes, E. Klein, S. Kull, M. M. R. Moayed, R. Lesyuk, C. Klinke, *Z. Phys. Chem.* **2018**, *232*, 1267.

[25] X. Xia, Y. Xia, *Nano Lett.* **2012**, *12*, 6038.

[26] F. Gerdes, C. Navío, B. H. Juárez, C. Klinke, *Nano Lett.* **2017**, *17*, 4165.

[27] S. Kull, L. Heymann, A. B. Hungria, C. Klinke, *Chem. Mater.* **2019**, *31*, 5646.

[28] C. Schliehe, B. H. Juarez, M. Pelletier, S. Jander, D. Greshnykh, M. Nagel, A. Meyer, S. Foerster, A. Kornowski, C. Klinke, *Science* **2010**, *329*, 550.

[29] P. Giannozzi, S. Baroni, N. Bonini, M. Calandra, R. Car, C. Cavazzoni, D. Ceresoli, G. L. Chiarotti, M. Cococcioni, I. Dabo, *J. Phys.: Condens. Matter* **2009**, *21*, 395502.

[30] X. Chen, D. Parker, D. J. Singh, *Sci. Rep.* **2013**, *3*, 3168.

[31] E. Burstein, S. Perkowitz, M. Brodsky, *J. Phys., Colloq.* **1968**, *29*, C4.

[32] L. Jones, H. Yang, T. J. Pennycook, M. S. Marshall, S. Van Aert, N. D. Browning, M. R. Castell, P. D. Nellist, *Adv. Struct. Chem. Imaging* **2015**, *1*, 8.